Original Research

Trenton E. Franz*
Jay Nolan
Jan M. Nordbotten
Kelly K. Caylor
Lee D. Slater

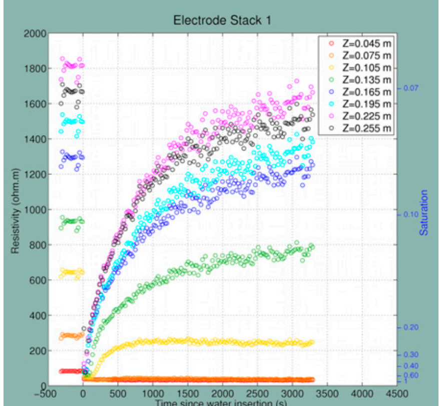

Observations from a dryland ecosystem link the distribution of vegetation with patterns of subterranean termite nests. In this laboratory study, we developed strategies to capture the general behavior of transient soil moisture dynamics generated in macropores. The strategies may help elucidate ecosystem behavior on larger spatial and temporal scales.

T.E. Franz, J.M. Nordbotten, and K.K. Caylor, Dep. of Civil and Environmental Engineering, Princeton Univ., Engineering Quad, Princeton, NJ 08544; J. Nolan and L.D, Slater, Dep. of Earth and Environmental Sciences, Rutgers Univ., Newark, NJ 07102. J.M. Nordbotten also at Dep. of Mathematics, Univ. of Bergen, N-5008 Bergen, Norway. *Corresponding author (tfranz@princeton.edu).

Vadose Zone J. 10:286–298
doi:10.2136/vzj2010.0031
Received 18 Feb. 2010.
Published online 14 Dec. 2010.

Quantifying Transient Soil Moisture Dynamics Using Multipoint Direct-Current Resistivity in Homogeneous Sand

Direct measurements of soil moisture are extremely difficult to obtain between the spatial scales of point measurements and remote sensing. Nevertheless, the spatiotemporal distribution of soil moisture remains a key variable in hydrology. In this study, we explored the use of multipoint direct-current resistivity to examine spatiotemporal changes in soil moisture following a rapid infiltration event into a large macropore. The methodology was selected because the time scale of flow processes in the homogeneous isotropic sand prevented the use of imaging techniques. Selection of an appropriate electrode array was critical for collecting the required high-resolution spatiotemporal resistivity measurements in a 1.44-m-diameter tank. Direct placement of a dense array of electrodes in the sand allowed us to use geostatistical methods for spatial interpolation, thereby removing the inherent uncertainty resulting from inversion mechanics (i.e., smoothness constraints for underconstrained problems). Instead, conversion of resistivity to saturation was directly performed using Archie's law. We compared the observations to a two-dimensional, axisymmetric, numerical solution of the system using the HYDRUS 2D/3D software, and to a semianalytical solution to estimate soil hydraulic properties. We found satisfactory comparisons among the observations and the numerical and semianalytical solutions of the system, which indicates that these techniques may be applicable to field-scale estimates of effective hydraulic properties. Subject to limiting initial conditions, boundary conditions, and material properties, the results of the semianalytical solution are encouraging for capturing general hillslope-scale dynamics at longer temporal scales toward a greater understanding of emergent patterns in dryland ecosystems.

Abbreviations: TDR, time domain reflectometry.

Despite the fact that space–time dynamics of soil moisture are a key variable in hydrology (Rodriguez-Iturbe and Porporato, 2004; Vereecken et al., 2008), direct estimates of soil moisture are difficult to obtain between the spatial scales of point measurements and remote sensing (Robinson et al., 2008). The field of geophysics has developed many interesting tools and techniques to fill those gaps where conventional methods are inadequate (Robinson et al., 2008), taking advantage of the relationship between electromagnetic properties and soil moisture in porous media (Archie, 1942; Topp et al., 1980). Given certain limitations and uncertainty, geophysical methods are often valuable tools for characterizing subsurface hydraulic properties (Binley et al., 2001; Hubbard et al., 2001). The use of a suite of tools has provided field-scale estimates of hydraulic properties that would be impossible to quantify with methods based on direct measurements of soil moisture alone (Binley et al., 2002; Cassiani and Binley, 2005; Lambot et al., 2006; Looms et al., 2008).

While the suite of available geophysical tools has provided unique opportunities in hydrology to understand natural processes that could not be observed by conventional methods alone, the myriad of geophysical methods has also caused significant confusion between the hydrologic and geophysical communities in experimental design and data interpretation (Ferré et al., 2009). State-of-the-art resistivity studies typically involve two- and three-dimensional inversion of large data sets and large parameter spaces (Furman et al., 2007; Koestel et al., 2008). Despite continued advances in the technology, there remain difficulties pertaining to the uncertainty and inherent nonuniqueness in the inversion mechanics involved in resistivity parameter estimation (i.e., regularization and smoothness constraints to stabilize underconstrained problems) (Binley and Beven, 2003; Day-Lewis and Lane, 2004; Day-Lewis et al., 2005; Jadoon et al., 2008). To address such problems, methodologies using multiple geophysical data sets (joint inversion) and advanced coupled inversion techniques have recently been developed (Furman et al., 2004; Brovelli et al., 2005; Kowalsky et al., 2005; Linde et al., 2006; Looms et al., 2008; Hinnell et al., 2010).

The current experiment was motivated by emergent system properties observed in a central Kenyan dryland ecosystem due to subterranean termite activity (Brody et al., 2010; Fox-Dobbs et al., 2010; Pringle et al., 2010). The spatial organization of woody vegetation and nutrient availability is regulated by the spatial arrangement of termite nests. At a single nest site, bioturbation of the soil by termites is extensive (Darlington, 2000, 2005), with numerous (10–20) open shafts (2–4 cm in diameter) extending several meters in the vertical and tens of meters in the horizontal. The horizontal extent of soil bioturbation at these termite mounds in central Kenya was visible from an electromagnetic induction survey, illustrating elevated electrical conductivities for 10 to 15 m radially around known nest sites (Franz, unpublished data, 2010). The impact of bioturbation and macropore activity has long been recognized as a substantial modifier of water balance flux terms and parameters at the scale of hillslopes (Beven and Clarke, 1986; Binley et al., 1989; Tsuboyama et al., 1994). In addition, the influence of macropores is ubiquitous, ranging from drylands (Turner, 2006) to humid regions (Sidle et al., 2001).

Despite their widespread influence, quantifying flow impacted by macropores remains a difficult research problem (Larsbo et al., 2005; Cey and Rudolph, 2009), especially at time scales longer than the individual rainfall event (Beven and Clarke, 1986; Weiler and Naef, 2003b; Leonard et al., 2004). To begin to understand the flow dynamics into the surrounding soil matrix and ecosystem impacts at larger spatial and longer temporal scales, we developed measurement and modeling techniques to capture the general behavior for subsurface flow originating in large macropores.

The objective of this study was to investigate the near-surface transient soil moisture dynamics using a direct-current resistivity approach (Telford et al., 1990; Rubin and Hubbard, 2005; Samouelian et al., 2005) while evaluating the geophysical data with different hydrologic modeling approaches. In a controlled laboratory setting using homogeneous isotropic sand, we simulated rapid water flow into an open shaft or large macropore that extended to an underlying impermeable layer. As a consequence of selecting homogeneous sand, we needed high-resolution space–time resistivity measurements to capture the transient behavior in the system. Because the motivation of the laboratory study was to understand the unsaturated flow processes and not necessarily the geophysical methodology, we placed the electrodes directly into the soil. The multipoint resistivity measurements were interpolated spatially using a geostatistical algorithm and converted to saturation using a petrophysical relationship (Archie, 1942) that is valid for medium to coarse grain sizes where surface conductivity is minimal (Friedman, 2005). The various hydrologic models, slug test (Hvorslev, 1951), numerical model (Šimůnek et al., 2006), semianalytical model (Nordbotten and Dahle, unpublished data, 2010), and geophysical data were compared by estimating the effective hydraulic model parameters for the system (Rucker and Ferré, 2004; Rucker et al., 2005; Hinnell et al., 2010).

Our results provided comparisons among the observations, numerical models, and semianalytical model solutions. We explored the potential applications and limitations of our methodology to field settings, parameter estimation and error analysis, and the potential use and limitations of semianalytical solutions describing flow dynamics generated in macropores.

Materials and Methods

Laboratory Setup

Soil moisture in the experiment was simplified to a function of two spatial dimensions (radius r and elevation z, assuming radial symmetry) and time t. To adequately capture the transient soil moisture dynamics, indirect estimates were collected using multipoint direct-current resistivity with direct placement of electrodes in the sand. A 10-channel resistivity meter (Syscal Pro, IRIS Instruments, Orleans, France) was used to collect the measurements at highly resolved spatial (∼2 cm) and temporal (∼20 s) scales per complete data set. The system contained three 48-wire panel units for a maximum of 144 possible electrode locations. Figure 1 illustrates the division of spatial and temporal scales that have been used with different geophysical techniques in the past. Initially, we considered using a single or multichannel imaging technique for the data collection given the desired spatial resolution; however, the length of time needed for data collection and inversion prevented the use of imaging techniques with even the fastest multichannel data acquisition systems with surface probes or from a limited number of boreholes given the short time scale of this rapid infiltration process. In contrast, capturing the detailed time scales would

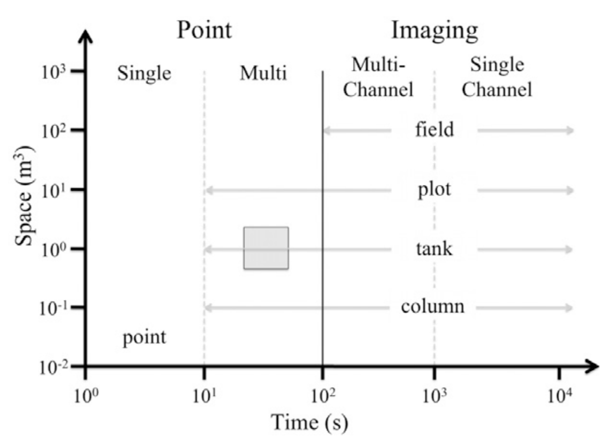

Fig. 1. Spatial and temporal scales of data collection using different geophysical techniques. The gray rectangle denotes the desired scale of observations for the current experimental laboratory design.

have been possible with point estimates such as time domain reflectometry (TDR). Without a more complex distributed sensor network (Robinson et al., 2008), the main disadvantage of TDR point measurements is the limited spatial coverage and resolution. At the intermediate spatial and temporal scales required to capture the flow processes in this experiment, rapid data acquisition with multipoint direct-current resistivity was deemed the best alternative.

Given the desired spatial and temporal sampling scales, the selection of the experiment geometry and electrode array was critical for accurately capturing the transient dynamics. Figure 2 illustrates the experimental geometry and water insertion well configuration. A circular plastic stock tank (1.44-m diameter, 0.45-m depth) was selected to maximize the distance from the well to the outer tank boundary. A 20-mm-thick rubber mat was placed in the bottom of the tank, which served as a level no-flow bottom boundary. To minimize material heterogeneities, homogeneous isotropic sand (ASTM 20/30, U.S. Silica Co., Ottawa, IL) was used throughout the tank. The sand particles were wet packed in the tank with efforts to minimize the buildup of fine particles between layers and to keep particle fall velocities consistent for uniform packing (Illangasekare, personal communication, 2008). The ASTM 20/30 sand was selected for its uniform particle size distribution (median particle diameter d_{50} = 0.54 mm, see Table 1) and spherical grain shapes for consistent packing. A cylindrical water insertion well (0.5-m height, 0.12-m diameter, with 2-mm-thick slots spaced every 20 mm vertically) was placed vertically in the tank center. The tank was placed on an adjustable level wooden platform (0.75-m height) with the ability to tip along one axis up to a 10° angle. Following the initial wet packing of the material, the tank was drained under gravity for 2 d. Using a piece of cylindrical metal sheeting (30-cm diameter), two depth profiles were excavated, with measurements of volumetric water content (Fig. 3a) and temperature (Fig. 3b) taken every 5 cm, 25 d after the tank was drained. Volumetric water content measurements were taken from grab samples (~200 g) at each depth by weighing the samples before and after drying (105°C for 24 h) in a convection oven. Soil temperature measurements were collected with a K2Dpro sensor (Decagon Devices, Pullman, WA). The initial saturation profile in the tank consisted of three distinct zones. The lowest zone (0–0.02 m) contained a layer near full saturation. The hydrostatic saturation profile in the middle zone (0.02–0.25 m) compared reasonably well with the reported parameter estimates using the Brooks–Corey relationship (Table 1) (Brooks and

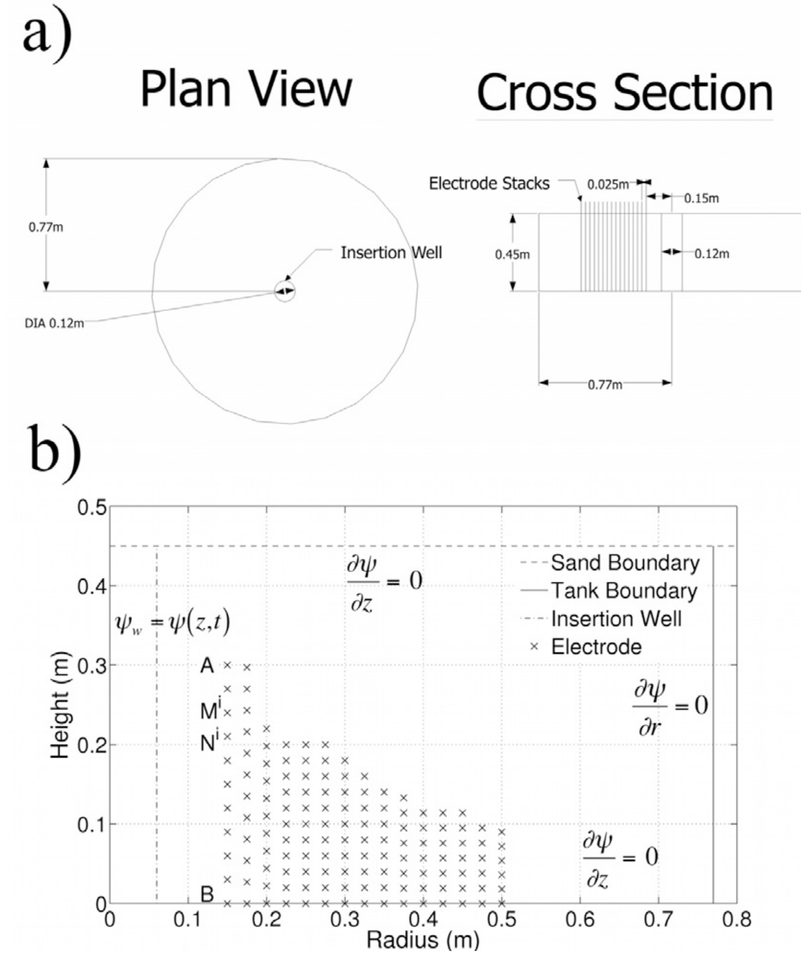

Fig. 2. Representation of experimental laboratory setup illustrating (a) the tank dimensions, geometry of the insertion well, and spacing of electrode stacks, and (b) spacing of individual electrodes (A and B are current electrodes, M and N are potential electrodes, r is the radius, ψ is the fluid potential, and ψ_w is the fluid potential at the insertion well–sand interface).

Table 1. Summary of constants and estimated parameters for the experiment using homogeneous sand.

Parameter	Value
Dry bulk density (ρ_b), g cm^{-3}†	1.57
Porosity (φ)†	0.406
d_{10}, mm†	0.41
d_{50}, mm†	0.54
d_{60}, mm†	0.6
Uniformity coefficient, d_{60}/d_{10}†	1.5
Pore size distribution index (λ)†	7.38
Residual volumetric water content (θ_r), cm^3 cm^{-3}†	0.039
Displacement pressure head (h_d), cm†	16.6
Saturated hydraulic conductivity (K_s), cm s^{-1}†	0.12
Resistivity of tap water at 18°C (ρ_w), Ω m‡	~5
Formation factor (F)‡	4.98
Saturation degree parameter (n_A)‡	1.623

† Values reported from (Sakaki and Illangasekare, 2007) for ASTM 20/30 sand (U.S. Silica Co., Ottawa, IL); d_{10}, d_{50}, and d_{60} are the diameters of which 10, 50, and 60%, respectively, of the grains are smaller.
‡ Values estimated during this study.

Corey, 1964; Sakaki and Illangasekare, 2007). The saturation profile in the highest zone (0.25–0.45 m) deviated from the Brooks–Corey relationship below the residual saturation point (0.10) due to dry ambient atmospheric laboratory conditions (20°C air temperature, 40% relative humidity) where surface evaporation modified the depth profile.

Electrode Array Configuration

Selection of the appropriate electrode array was a crucial step in obtaining high-resolution space–time data. Given the water insertion volume and material hydraulic properties, a simple analytical solution of the unsaturated flow in the experimental system (Huppert and Woods, 1995; Barenblatt, 1996) was used to constrain the distribution of electrodes, maximizing the spatial resolution of measurements. Figure 2 illustrates the geometry of the tank and water insertion well (Fig. 2a) and the electrode stack locations, with the coordinates of each electrode relative to the center of the water insertion well (Fig. 2b). Copper wire (20 AWG, 0.812-mm diameter) was wrapped around a composite plastic rod (diameter = 9.525 mm) and inserted vertically into the sand at the specified spatial locations following initial drainage of the tank. Figure 2b illustrates the electrode array used for injecting current and taking potential measurements. We selected an asymmetric α type array, adopting the classification system proposed by Szalai and Szarka (2008), for two reasons. The first reason was to minimize the number of changes in current location, taking advantage of simultaneous potential measurements offered by the 10-channel system. Current was injected at each end of the electrode stack, probes A and B. While the current was being injected, potential measurements between probes M and N were collected simultaneously along the electrode stack at nine locations (between 10 probes). By limiting the number of electrodes per stack to 12, only one current injection per electrode stack was required, thereby minimizing the collection time. The second reason was to avoid taking a potential measurement following current injection at the same electrode. Surface charges can build up at the probe–soil interface and lead to erroneous readings unless precautions are used to discharge the system (Dahlin, 2000). Data were collected cyclically at all 15 electrode stack locations with a time resolution of 1.4 s per electrode stack and 21 s per complete data set (Table 2). A known volume of water was inserted into the system approximately 5 min after measurements began. The resistivity measurements were taken up to 55 min after water insertion. To simplify data visualization and analysis, all measurements during one electrode stack sampling cycle were assigned one mean time. This allowed the data to be presented and analyzed as two-dimensional time slices. The resistivity point data were then interpolated into a spatially continuous field (r, z) by an ordinary kriging method for each time slice.

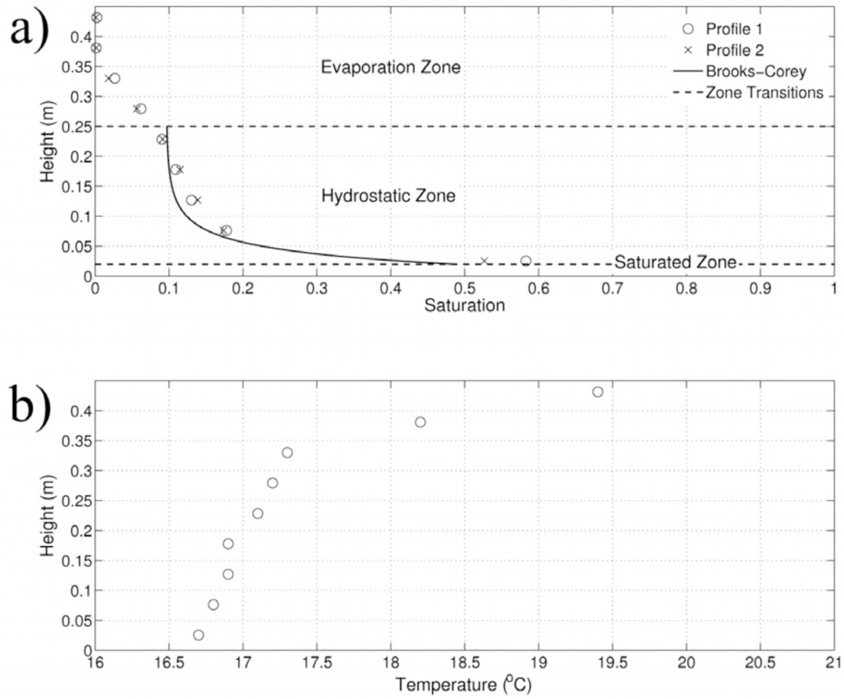

Fig. 3. (a) Initial saturation and (b) temperature depth profiles of conditions inside the tank following gravity drainage. Three distinct zones were present in the saturation profile. The lowest zone was a fully saturated layer, the middle zone roughly followed the Brooks–Corey relationship for the material, and evaporation influenced the highest zone.

Table 2. Summary of experimental water insertion test, where measurements were collected with a 10-channel resistivity meter.

Parameter	Value
Electrode array type†	α type, asymmetrical
Number of electrodes	144 max.
Current injection length per stack, s	0.15
Measurement period of 1 electrode stack, s (max. of 12 electrodes)	~1.4
Changes in current location per complete data set	15
Number of resistivity measurements per complete data set	90
Temporal resolution per complete data set, s	~21
Spatial resolution, m	~0.02
Insertion water volume, m^3	0.02
Duration of water insertion, s	~25
Insertion water temperature, °C	16

† Classification scheme adopted from Szalai and Szarka (2008).

Correction of Resistivity Data in Bounded Domains

The experimental setup consisted of continuous current flow through an isotropic homogeneous medium. Using Ohm's law and assuming no charge accumulation, the electrical potential around a single set of buried electrodes not influenced by boundaries is (Telford et al., 1990)

$$V = \left(\frac{I\rho}{4\pi}\right)\frac{1}{r} \quad [1]$$

where V (V) is the scalar potential, ρ (Ω m) is the resistivity of the medium and also the reciprocal of the conductivity σ (S m^{-1}), and r (m) is the distance from the current source to the potential electrode.

In practice, direct-current resistivity surveys require four electrodes, two current (A and B) and two potential (M and N) (Fig. 2b). Due to the geometry of the electrodes and boundary conditions, the distance term r in Eq. [1] is a more complex coefficient. The cylindrical experimental system consisted of no-flow boundary conditions. To simplify the potential field, we treated the domain as a bounded infinite plane by assuming that the measurements were not greatly affected by the tank outer boundaries and the relatively small water insertion well. We were able to correct each electrode configuration for the closer tank upper and lower no-flow boundaries, however, by deriving a closed-form solution to the Laplace equation using the method of images (Haberman, 1998). The infinite series solution can be rewritten as

$$V = \left(\frac{I\rho}{4\pi}\right)\left[\sum_{n=0}^{\infty}\left(\frac{1}{(-1)^n A - M + \left\{\left[\frac{1+(-1)^{n+1}}{2}\right]+n\right\}D}\right) + \sum_{n=1}^{\infty}\left(\frac{1}{(-1)^{n-1} A + M + \left\{\left[\frac{1+(-1)^{n}}{2}\right]+n-1\right\}D}\right) - \sum_{n=0}^{\infty}\left(\frac{1}{(-1)^{n+1} B + M + \left\{\left[\frac{1+(-1)^{n}}{2}\right]+n-1\right\}D}\right) - \sum_{n=1}^{\infty}\left(\frac{1}{(-1)^{n} B - M + \left\{\left[\frac{1+(-1)^{n+1}}{2}\right]+n\right\}D}\right)\right] \quad [2]$$

where D (m) is the distance between the no-flow boundaries, A (m), B (m), and M (m) are the distances from the A, B, and M electrodes, respectively, to the lower no-flow boundary, and n is the number of terms (levels of image sources and sinks) to include from 0 to ∞. The first two terms are the result of the image sources from the positive current source A and the last two terms are the result of the negative current sink B. When n is equal to zero, Eq. [2] reduces to the simplified form reported in many texts (Heiland, 1940; Jakosky, 1950; Telford et al., 1990). Given the geometry of the system, inclusion of the first two terms (n = 2) in Eq. [2] results in relative changes of <1% for all electrode arrays in the system. The small relative changes suggest that, given the distance from the outer boundary to each electrode (minimum distance of 27 cm), the outer boundary has minimal influence on the individual electrodes' potential field.

Measurement errors were evaluated by comparing the normal resistance measurements, R_N (Ω), with the reciprocal measurements, R_R (Ω). Given the speed of the process and limitations of the instrumentation data collection times, reciprocal measurements were not feasible to collect for every time frame. To obtain an idea about the measurement errors in the tank, however, we collected reciprocal measurements before the infiltration event. The deviations of absolute values from a perfect array illustrate normal behavior (logarithmically transformed) with a mean deviation of <1.8% (Fig. 4a). The cumulative distribution function indicated that 85% of

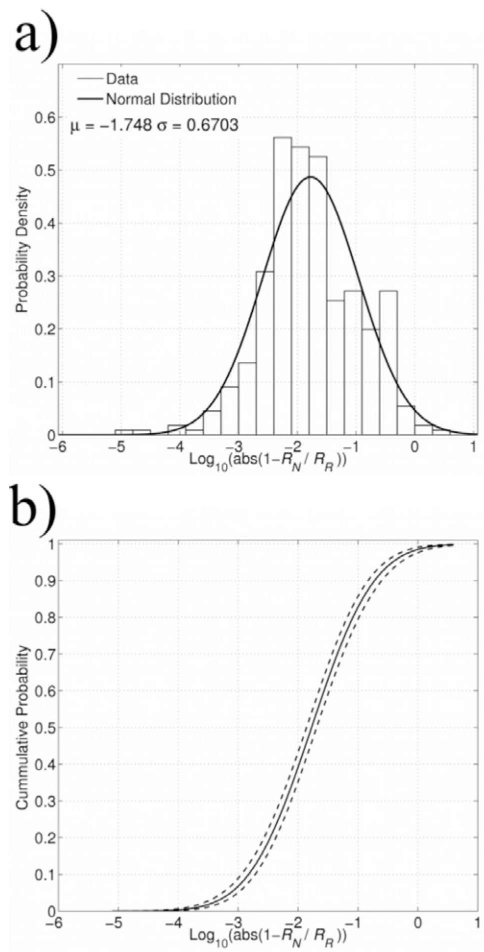

Fig. 4. (a) Probability density and (b) cumulative probability of absolute deviations between normal resistivity (R_N) and reciprocal resistivity (R_R) measurements of the 90 electrode arrays used in the experiment (n = 180).

the measurements had an error of <10% (Fig. 4b). In addition, the covariance matrix between measurement error and experimental geometry revealed very weak correlations, with a maximum value of 0.063 between the radial distance of measurement and measurement error. Despite evidence of changing error values with resistivity (Koestel et al., 2008), the correlation between measurement error and fluid saturation was small: 0.055. The lack of correlation observed in this experiment was probably due to the small support volumes that would not be greatly distorted as fluid saturation changes. Finally, we note that the uncertainty in the resistivity data measurements is small compared with the uncertainty in the applied petrophysical model that is discussed below.

Conversion of Resistivity to Saturation

The relationship between electrical resistivity and saturation, known as Archie's law, is a key equation for use in indirect methods such as direct-current resistivity (Archie, 1942; Samouelian et al., 2005; Robinson et al., 2008). Combining Archie's law and information about the pore geometry results in the relationship between resistivity and saturation, defined as (Archie, 1942; Samouelian et al., 2005)

$$S=\left(\frac{F\rho_{\mathrm{w}}}{\rho_{18}}\right)^{1/n_A} \quad [3]$$

where S (dimensionless) is the degree of saturation from the available pore space, F (dimensionless) is the true formation factor of the saturated material, n_{A} (dimensionless) is the saturation degree parameter, ρ_{w} (Ω m) is the electrical resistivity of injected water corrected to 18°C, and ρ_{18} (Ω m) is the temperature-corrected resistivity to 18°C (Table 1). Because resistivity measurements are a function of temperature, the following correction was made due to the temperature gradient in the tank as a result of ambient laboratory conditions (Campbell et al., 1948):

$$\rho_{18}=\left[\frac{\rho(T)}{1+\alpha(T-18)}\right] \quad [4]$$

where $\rho(T)$ (Ω m) is the electrical resistivity collected at temperature T (°C) and α (°C^{-1}) is a coefficient assumed equal to 0.025. Figure 5a illustrates the laboratory results using a column of the homogeneous sand and various fluid conductivities of a KCl solution. The inverse of the slope of the linear relationship is the true saturated formation factor, F, and the y intercept represents the surface conductivity, which was found to be negligible. Figure 5b illustrates the relationship between saturation and resistivity, with the calibrated best-fit line using the observed values in the tank following gravity drainage. We note that the best-fit line was forced through the resistivity value of fully saturated sand (25 Ω m) by knowing the true saturated formation factor and the resistivity of water.

Numerical Solution of Subsurface Flow

The numerical approximation of unsaturated and saturated subsurface flow for the two-dimensional axisymmetric experimental system was calculated with a commercial software package (HYDRUS 2D/3D, PC-Progress, Prague, Czech Republic) (Šimůnek et al., 2006, 2008). The governing equation was subject to the following initial condition, IC:

$$\mathrm{IC}(r,z,t)=\begin{cases}\theta=\theta_{\mathrm{s}} & r,0\le z\le z_{\theta_s},0\\ \theta=\theta_{\mathrm{BC}}(z) & r,z_{\theta_s}<z\le Z,0\end{cases} \quad [5]$$

where θ_{s} (cm^3 cm^{-3}) is the saturated water content assumed equal to the sand porosity, $z_{\theta\mathrm{s}}$ (m) is the height of the saturated layer, $\theta_{\mathrm{BC}}(z)$ (cm^3 cm^{-3}) is the volumetric water content determined by the Brooks–Corey equation (Brooks and Corey, 1964), and Z (m) is the location of the sand–atmosphere boundary (Fig. 3a). Hydraulic relationships were estimated by the Brooks–Corey equation (Brooks and Corey, 1964). The system boundary conditions are described in Fig. 2b, with the note that as the water level dropped in the insertion well, the interface returned to a no-flow boundary condition. In addition to the forward solution, we used the software's inverse solution option (Šimůnek et al., 2006) to estimate the two shape parameters in the Brooks–Corey model, α_{BC} (cm^{-1}) and n_{BC} (dimensionless), and the saturated hydraulic conductivity K_{s} (cm s^{-1}). We used 600 resistivity observations

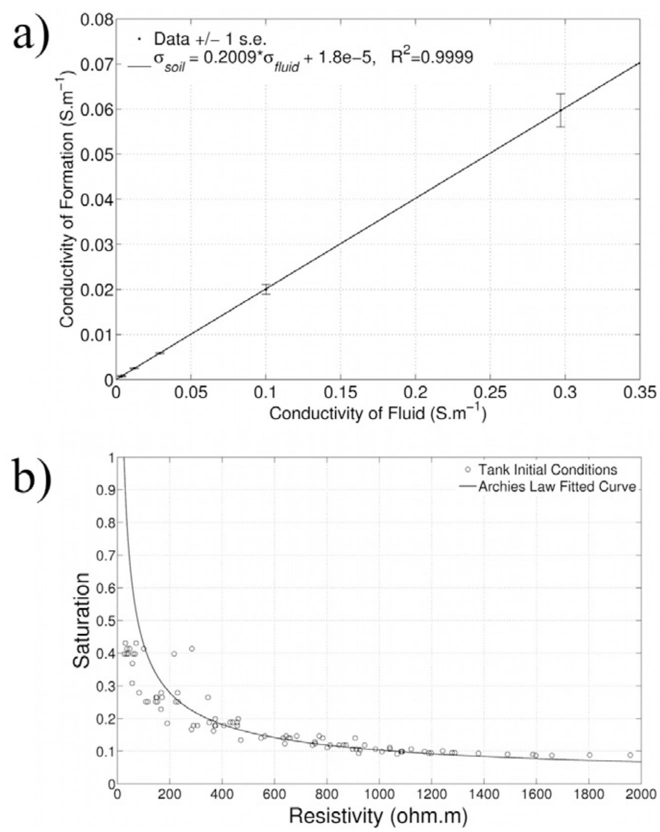

Fig. 5. (a) Derivation of the true saturated formation factor F (inverse slope of linear relationship) of the material using a column of homogeneous sand and a range of fluid conductivities; and (b) conversion between resistivity and saturation parameterized using the formation factor and measurements of tank initial conditions using Archie's law (Archie, 1942).

from 29 electrode locations (Electrode Stacks 1, 4, 8, 12, and 15) collected during the first 400 s to estimate the parameter mean values and confidence intervals.

Semianalytical Solution of Subsurface Flow

A variety of applicable graphical (Hvorslev, 1951; Pinder and Celia, 2006) and analytical (Philip, 1969; Huppert and Woods, 1995; Tracy, 1995; Barenblatt, 1996; Wu and Pan, 2005) models exist for the simple experimental system. Assuming that the system behaves like an unconfined aquifer, a simple graphical method using information about the changing water level in the insertion well (Hvorslev, 1951; Pinder and Celia, 2006) was used to estimate the saturated hydraulic conductivity. In addition, a large class of analytical solutions has been developed by the use of the Boltzmann transformation (Philip, 1969; Hillel, 1998; and references therein) to reduce the complexity of the governing partial differential equation.

With respect to the current experiment, we used the Boltzmann transformation to describe the flow of water over a flat, unbounded impermeable layer in homogeneous sand. Assuming a sharp interface condition, a simple closed-form radial solution exists for the transient collapse of the water mound (Barenblatt, 1996):

$$h(r,t)= \begin{cases} \left(\dfrac{Q^{1/2}}{16K_s^{1/2}t^{1/2}}\right)\left[8-\dfrac{r^2}{(QK_st)^{1/2}}\right] & r\le\sqrt{8}(QK_st)^{1/4} \\ 0 & r>\sqrt{8}(QK_st)^{1/4} \end{cases} \quad [6]$$

where h (m) is the height of the water mound, $Q = V_w/2\pi\varphi$ (m^3), V_w (m^3) is the volume of the water mound, and φ is the porosity (cm^3 cm^{-3}).

While the sharp interface condition is necessary for a closed-form solution, a more complete description of the unsaturated zone was necessary for the experiment. Multiscale modeling frameworks have been developed in which the vertical profile of water saturation is reconstructed in the context of vertically averaged models (Lake, 1989; Nordbotten and Dahle, unpublished data, 2010). When the system is in vertical equilibrium, the vertical saturation profile can be reconstructed from the hydrostatic profile using the unsaturated hydraulic relationships. For the current experiment, however, the rapidly changing height of the water table would cause significant deviations in the hydrostatic profile.

The vertical saturation profile is controlled by the local vertical pressure gradient (Pinder and Celia, 2006). Examination of the vertical form of Darcy's law,

$$q_z=-K_s\left(\frac{1}{\rho_w g}\frac{\partial P}{\partial z}+1\right) \quad [7]$$

illustrates the consequences of the vertical fluxes on the pressure gradient and subsequent height of the capillary fringe, H_{CF}:

$$\begin{cases} q_z=0, & \dfrac{\partial P}{\partial z}=-\rho_w g, \; H_{CF}=\text{hydrostatic} \\ q_z>0, & \dfrac{\partial P}{\partial z}<-\rho_w g, \; H_{CF}<\text{hydrostatic} \\ q_z<0, & \dfrac{\partial P}{\partial z}>-\rho_w g, \; H_{CF}>\text{hydrostatic} \end{cases} \quad [8]$$

where P is the fluid pressure (Pa), z is positive upward, q_z (m s^{-1}) is the vertical flux of water, ρ_w (kg m^{-3}) is the density of water, and g (m s^{-2}) is the gravitational constant. Using the analytical solution (see Eq. [6]; Barenblatt, 1996), we can estimate the local pressure gradient at all points along the radial profile:

$$\frac{\partial P}{\partial z}=-\rho_w g\left(\frac{\phi\partial h}{K_s\partial t}+1\right) \quad [9]$$

where ϕ is the porosity (cm^3 cm^{-3}), h (m) is the local change of height in the water table, and t is time (s). The vertical saturation profile and dynamic hydraulic shape parameters (α and n) can be estimated from (Pinder and Celia, 2006)

$$H_{P_i}=\frac{P_i(S_i)-P_{WT}}{\partial P/\partial z} \quad [10]$$

where H_{P_i} (m) is the height of the desired pressure (saturation) interval, $P_i(S_i)$ (Pa) is defined by the hydraulic model, and P_{WT} (Pa) is the water table pressure, which is equal to 0. With the known dynamic hydraulic shape parameters, the numerical vertical reconstruction of saturation distribution can be performed (Nordbotten and Dahle, unpublished data, 2010). We note that the vertical reconstruction is subject to mass balance, and an upper limit on the dynamic hydraulic parameters were set such that capillary fringe heights did not exceed the depth of the tank.

Results

As a simplification for data analysis and visualization, we present our results in two spatially continuous dimensions (r and z) and at averaged discrete points in time. The spatial fields were constructed from the 90 time series of resistivity point data using a geostatistical algorithm (ordinary kriging). The discrete points in time were assigned the mean time during one complete data set collection period (resolution 21 s). Figure 6 illustrates the time series of resistivity data for eight depths at the electrode stack nearest to the insertion well (r = 0.15 m). The time series illustrates the two steady states of the system and the transient response between the two states. Before water insertion, the resistivity data showed the initial soil moisture depth profile at the electrode stack, which consisted of three distinct zones (Fig. 3a). Directly following water insertion, all resistivity values dropped to near fully saturated

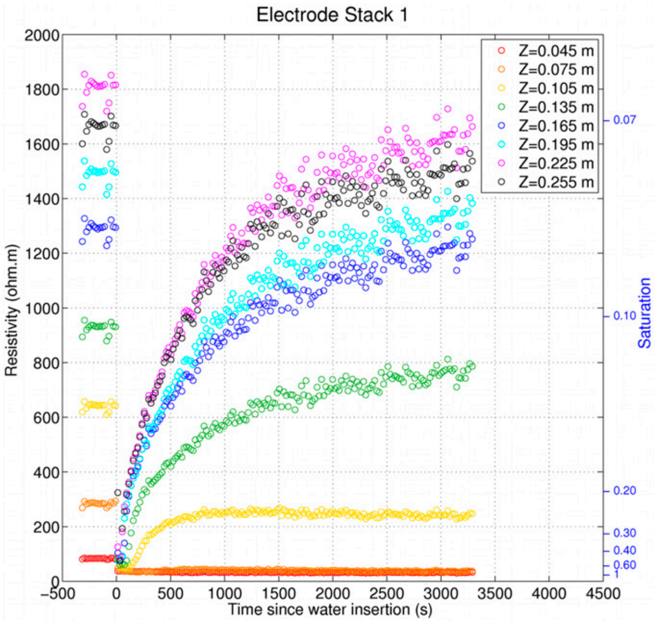

Fig. 6. Time series of resistivity and saturation values for Electrode Stack 1 (radius $r = 0.15$ m) for eight depths (z) along the profile collected during the water insertion test.

conditions (25 Ω m), with some dropping by nearly two orders of magnitude. Depending on the depth, the resistivity values either remained at fully saturated values or followed a distinct parabolic shape to a new steady-state resistivity value dependent on the new water content. The time series of resistivity values demonstrates that most of the transients occurred during the first 500 s, with relatively small changes in saturation afterward.

After applying Archie's law and interpolating the point data spatially, the left-hand columns in Fig. 7, 8, and 9 illustrate the saturation field at several different time slices. The series of images shows the invasion and collapse of the saturated mound to the new steady-state conditions in the tank. The observational data reveal that the mound remained mostly intact during the experiment and the transition zone from saturated to unsaturated conditions was fairly small (∼0.01–0.03 m) for most of the observations. The role that changing pressure forces played in the dynamic capillary fringe was discussed above (see Eq. [7–10]).

The middle columns of Fig. 7, 8, and 9 illustrate the numerical solution of the system and correlation coefficient, R^2 (pixel by

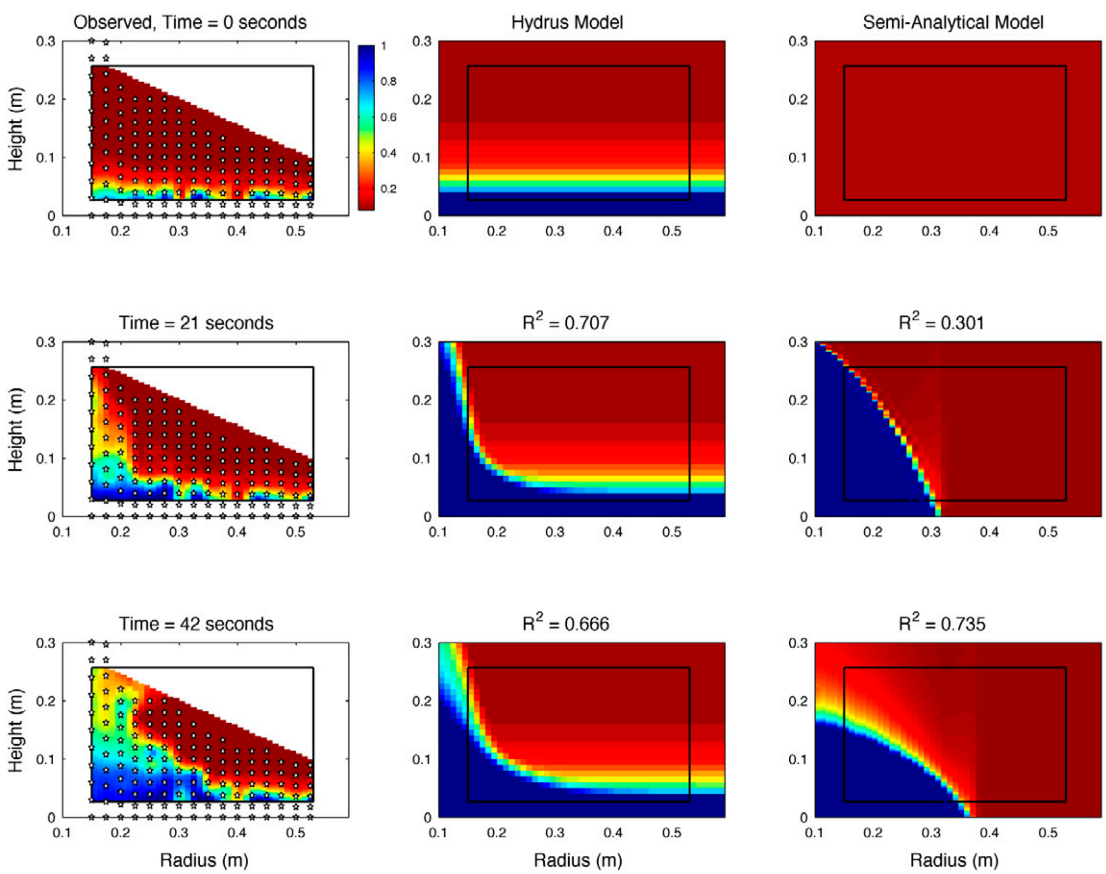

Fig. 7. Space–time tank saturation images at 0, 21, and 42 s (red = residual saturation, blue = fully saturated) after water insertion: an ordinary kriging interpolation method of the point data (electrode locations shown by white star pentagons) was used to generate the spatial fields at each time interval (left); constructed with the numerical solver HYDRUS 2/3D for the axisymmetric transient flow problem (Šimůnek et al., 2008) (middle); and constructed with a semianalytical solution (Barenblatt, 1996; Nordbotten and Dahle, 2010) (right).

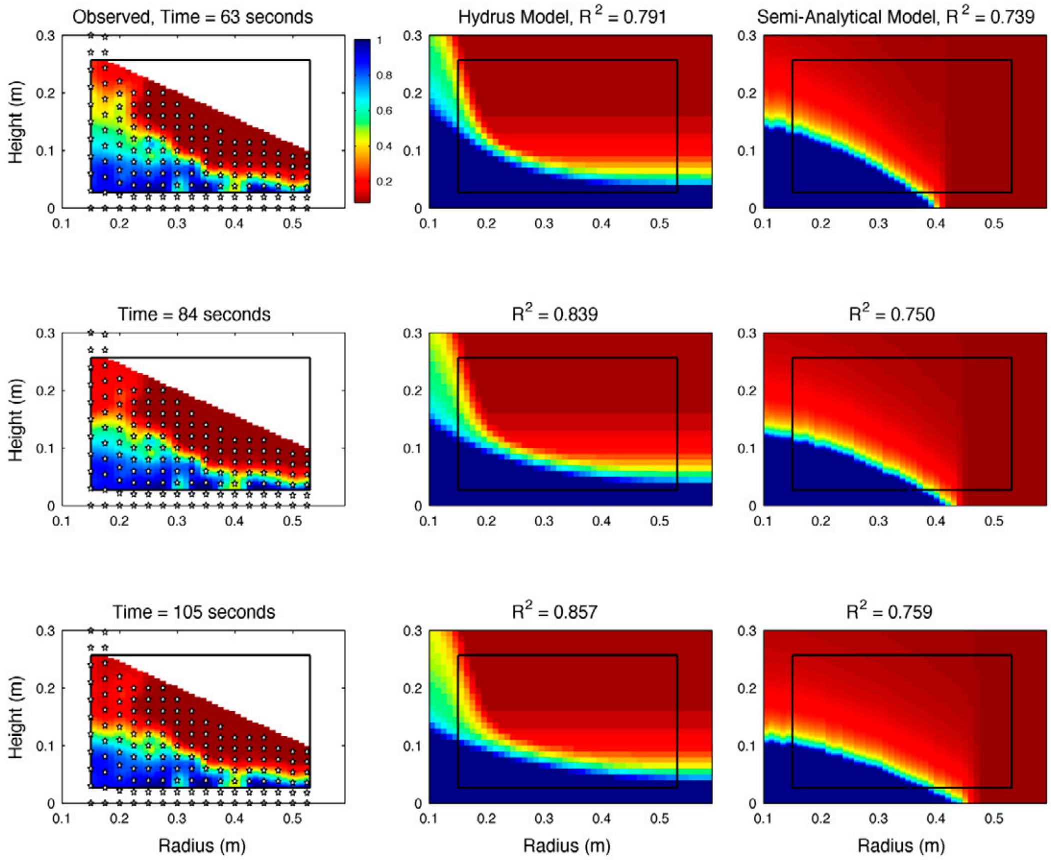

Fig. 8. Space–time tank saturation images at 63, 84, and 105 s (red = residual saturation, blue = fully saturated) after water insertion: an ordinary kriging interpolation method of the point data (electrode locations shown by white star pentagons) (left); HYDRUS 2/3D solution (middle); and semi-analytical solution (right).

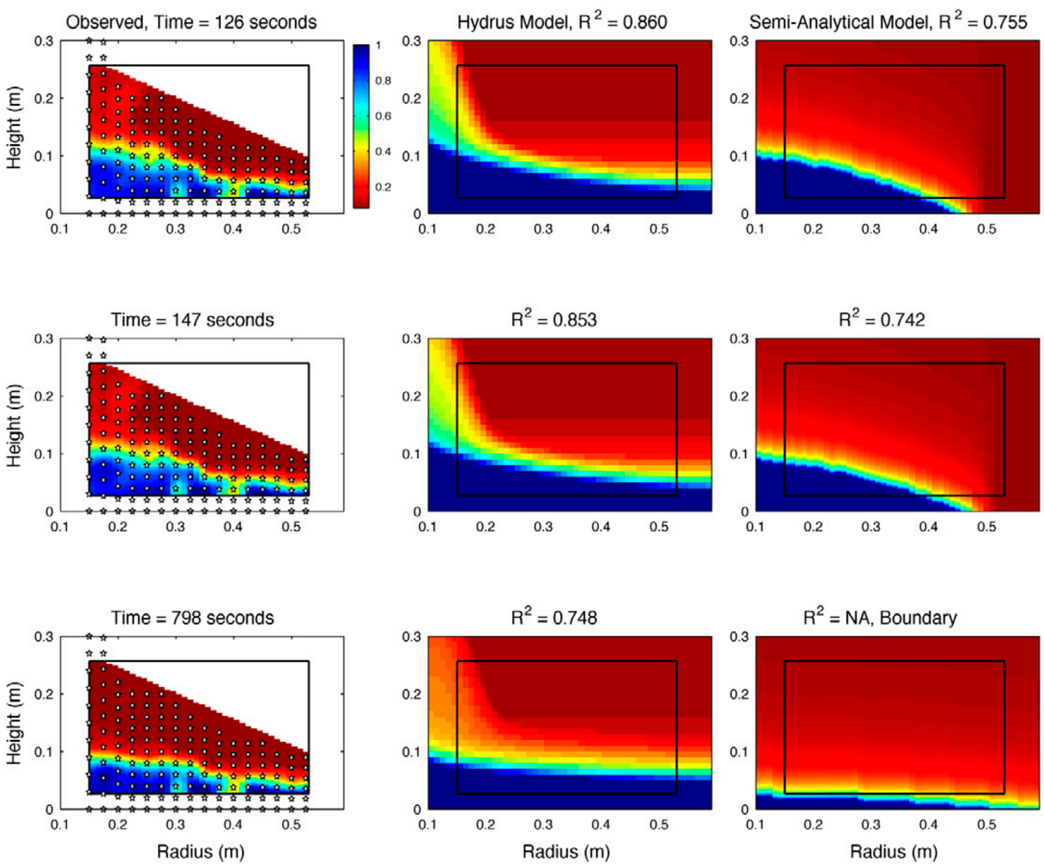

Fig. 9. Space–time tank saturation images at 126, 147, and 798 s (red = residual saturation, blue = fully saturated) after water insertion: an ordinary kriging interpolation method of the point data (electrode locations shown by white star pentagons) (left); HYDRUS 2/3D solution (middle); and semianalytical solution (right). NA = not applicable.

Table 3. Summary of estimates of the Brooks–Corey unsaturated flow parameters saturated hydraulic conductivity (K_s) and shape parameters α_{BC} and n_{BC}, and correlation with observations for the homogenous sand found using an inverted numerical model constrained by observations (HYDRUS 2D/3D), a semianalytical model (Nordbotten and Dahle, 2010), a slug test (Hvorslev, 1951), and values reported in the literature (Sakaki and Illangasekare, 2007).

Parameter estimation method	K_s	α_{BC}	n_{BC}	Mean R^2 during transient response (30–200 s)
	cm s^{-1}	cm^{-1}		
HYDRUS 2/3D	0.105	0.4072	1.296	0.818
Semianalytical	0.089	NA†	NA	0.744
Hvorslev fit‡	0.079	NA	NA	NA
Literature§	0.12	0.0602	0.5917	0.070

† NA, not applicable.
‡ Solution was found using the AQTESOLVE software (Pinder and Celia, 2006) for an unconfined aquifer using data from Electrode Stack 1.
§ Estimated from values reported in Sakaki and Illangasekare (2007).

pixel comparison for each data set) following model calibration with the Brooks–Corey hydraulic functions (Brooks and Corey, 1964; Šimůnek et al., 2006, 2008). The low correlation coefficient at 21 s indicates that time smearing was significant in the observational data due to the rapidly changing profile. Using the observational data set as input for the inverse solution, best-fit values of the hydraulic parameters are presented in Table 3. Estimates of K_s between the numerical results (0.105 cm s^{-1}), the literature (0.12 cm s^{-1}) (Sakaki and Illangasekare, 2007), and a slug test (0.079 cm s^{-1}) (Hvorslev 1951) were fairly consistent (Table 3); however, estimates of the hydraulic function shape parameters α_{BC} and n_{BC} were significantly different. Physically, these parameters control the length and steepness of the transition zone between the unsaturated and saturated zones. A sensitivity analysis of the hydraulic parameter estimates indicated that K_s was the least sensitive due to the wide 95% confidence intervals (K_s = 0.0664 and 0.1442 cm s^{-1}, α_{BC} = 0.3913 and 0.4231 cm^{-1}, n_{BC} = 1.267 and 1.325).

The right-hand columns of Fig. 7, 8, and 9 illustrate the semianalytical solution to the system (Barenblatt, 1996; Nordbotten and Dahle, unpublished data, 2010) and correlation coefficients following calibration. The estimate of K_s (0.089 cm s^{-1}) compares well with the other methods (Table 3). The semianalytical solution is an idealization of the system because of simplified initial conditions, source term, and outer boundary condition. Despite the limitations, the semianalytical solution provided reasonable results (R^2 =0.744) compared with the numerical solution (R^2 = 0.818) at early times (30–200 s) (Table 3). The results of the parameterization, experimental error, and correlation between the various methods are discussed further below.

Discussion

At spatial and temporal scales between point estimates (i.e., TDR) and imaging techniques (i.e., electrical resistivity tomography), multipoint direct-current resistivity has the potential for collecting high-resolution space–time measurements (Fig. 1). As was the case with the current experimental study, certain hydrologic settings will prohibit the use of imaging techniques due to the time requirements for data collection and inversion, which were too great to capture the essential space–time processes. While this experiment only considered homogenous porous media, construction of a detailed space–time history of saturation is critical for understanding and dissecting the inherent nonuniqueness in heterogeneous systems to estimate unsaturated hydraulic parameters (Pinder and Celia, 2006; Looms et al., 2008; Koestel et al., 2009). The detailed space–time data provided by this technique could be used to provide estimates of effective hydraulic parameters at larger spatial scales (Thomasson et al., 2006; Durner et al., 2008; Besson et al., 2010) and validation of three-dimensional models. The main limitations of the method (relative to inversion using only surface electrodes) are insertion of the electrodes to the desired depths, the possible formation of preferential flow paths, and potentially poor electrode contact under dry conditions. Ideal settings for the methodology are sandy or soft soils, such as the sands along the Kalahari Transect (Williams and Albertson, 2004), or the soft soils in northern peatlands (Slater and Reeve, 2002). Regardless of the desired field application, the methodology provides another tool in the ever-expanding geophysical tool set used for understanding physical processes (Robinson et al., 2008).

In addition to collecting high-resolution data, the current study investigated different modeling approaches used to estimate hydraulic parameters in the system. Due to the low sensitivity of saturated hydraulic conductivity, all three modeling techniques provided reasonable estimates (Table 3). Given the simplicity of the estimation technique and data collection, the slug test provided satisfactory results for the parameter estimation of saturated hydraulic conductivity for this experiment. In contrast, the inverse numerical technique was the only method capable of providing estimates of the hydraulic shape parameters, which differed significantly from literature estimates (Table 3). The discrepancy in shape parameter estimates was due to the small vertical length between the saturated and unsaturated zones because only observational data from the transient phase of the experiment was used in the calibration. The large grain size of the homogeneous sand led to the rapid collapse of the water mound and compressed height of the capillary fringe along the leading edge (see Eq. [7–10] and Fig. 7, 8, and 9).

Comparison of the observations with the numerical solution indicate a total error (sum of measurement, moisture content estimation, and model error) around 18% for the experiment. Measurement error was estimated by reciprocal measurements with a mean value around 1.8% (Fig. 4). Data were analyzed at discrete time slices, causing significant time smearing at 21 s that diminished at successive intervals (Fig. 7, 8, and 9, left-hand columns). The most significant source of error came from the conversion of resistivity to saturation at intermediate saturation values (Fig. 5b) because the relationship was constrained at full saturation by knowing the true saturated formation factor and resistivity of water (Fig. 5a). The combined error from measurements and moisture content estimation for the experiment is estimated around 5 to 10%. Contributions to the remaining error were due to the unsaturated flow well boundary condition, deviation of flow from Darcy's law at early times, negligence of hysteresis in the hydraulic model, and material heterogeneities. The most significant source of model error was due to the well boundary condition because water was added during a finite interval instead of instantaneously (Table 2). At early time (<10 s), velocities near the insertion well resulted in Reynolds numbers slightly greater than unity ($\sim$1.5) and departure from Darcy's law (Bear, 1972; Hillel, 1998). After 10 s, all velocities resulted in Reynolds numbers less than unity. Following wetting of the sand, hysteretic affects will cause the saturation profile to collapse faster than currently calculated with the Brooks–Corey relationship (Fig. 7, 8, and 9). We decided not to include hysteretic affects to directly compare numerical parameter estimates with literature estimates for the homogeneous sand (Sakaki and Illangasekare, 2007). More advanced models that include hysteresis (such as the van Genuchten–Mualem model) may be used in the HYDRUS 2/3D framework (Šimůnek et al., 2008).

The motivation for the current study was to evaluate the use of measurement and modeling strategies for understanding the impacts of flows generated by large macropores into the surrounding soil matrix. Of particular interest was the influence that subterranean termites have on ecological patterns in dryland ecosystems (Turner, 2006; Brody et al., 2010; Fox-Dobbs et al., 2010; Pringle et al., 2010). Pattern formation of woody vegetation in dryland ecosystems requires spatial and temporal soil moisture dynamics on the scale of decades and centuries (Rodriguez-Iturbe and Porporato, 2004; D'Odorico and Porporato, 2006), beyond the feasible capacity of current macropore models (Weiler and Naef, 2003b; Leonard et al., 2004). The results of the semianalytical framework for this study are encouraging for describing the general flow behavior generated by large macropores subject to the limiting initial conditions, boundary conditions, and material properties. At early times (<300 s) before the outer tank boundary substantially influenced flow, the main difference between the numerical and semianalytical models was the initial conditions in the tank (Fig. 3a and 7, 8, and 9, left-hand columns). Correlation results with the observations indicate a loss of $\sim$7% of information between the numerical and semianalytical models (Table 3). We were primarily interested in the effects of large macropores in the near surface of dryland ecosystems where water tables are relatively deep and the impacts to initial saturation profiles at the beginning of the rainy season would be minimal. As studies move to real ecosystems, an understanding of subsurface properties (i.e., the spatial structure of macropores, depth to bedrock, soil heterogeneity) will be critical for the appropriate use of the semianalytical framework. Coupling the measurements with macropore dye studies (Weiler and Naef, 2003a; Weiler and Flühler, 2004; Cey and Rudolph, 2009) may prove informative for understanding the impacts of macropores on the redistribution of subsurface water (Weiler and Naef, 2003b; Leonard et al., 2004) and nutrients (Cey et al., 2009).

Conclusions

Despite the limitations of the controlled experimental setting, the multipoint direct-current resistivity technique has the potential to increase understanding of flow processes at field scales but needs to be tested. Given the inherent heterogeneities in natural systems, the conversion of resistivity to saturation via a simple Archie's petrophysical relationship is unlikely to be valid. In addition, layering of soil horizons may cause substantial shifts in the potential field, which will need to be taken into account. In such cases, the detailed resistivity measurements may provide a valuable constraint in a coupled hydrogeophysical inversion procedure because the point measurements are collected at known depths.

The use of semianalytical models in a parsimonious water balance framework has the potential for greater understanding of the effects of macropore-generated subsurface flow on the long-term vegetation dynamics of water-limited ecosystems. While the use of analytical and semianalytical solutions depends on appropriate system initial conditions, boundary conditions, and material properties, the potential computation savings for simulating processes at longer time scales remains enormous.

Acknowledgments

We would like to thank Alex Furman, Ty Ferré, Michael Celia, Luke MacDonald, and Elizabeth King for their various contributions that improved this manuscript. K.K. Caylor and T.E. Franz would like to thank NSF OISE-0854708 and the Princeton University Walbridge and Technology for Developing Regions Fellowships for their financial support. Equipment used in this project was supported by the National Science Foundation under Grant EAR-0732250.

References

Archie, G.E. 1942. The electrical resistivity log as an aid in determining some reservoir characteristics. Trans. Am. Inst. Min. Metall. Eng. 146:54–61.

Barenblatt, G.I. 1996. Scaling, self-similarity, and intermediate asymptotics. Cambridge Univ. Press, New York.

Bear, J. 1972. Dynamics of fluids in porous media. Elsevier, New York.

Besson, A., I. Cousin, H. Bourennane, B. Nicoullaud, C. Pasquier, G. Richard, A. Dorigny, and D. King. 2010. The spatial and temporal organization of soil water at the field scale as described by electrical resistivity measurements. Eur. J. Soil Sci. 61:120–132.

Beven, K.J., and R.T. Clarke. 1986. On the variation of infiltration into a homogeneous soil matrix containing a population of macropores. Water Resour. Res. 22:383–388.

Binley, A., and K. Beven. 2003. Vadose zone flow model uncertainty as conditioned on geophysical data. Ground Water 41:119–127.

Binley, A., K. Beven, and J. Elgy. 1989. A physically based model of heterogeneous hillslopes: 2. Effective hydraulic conductivities. Water Resour. Res. 25:1227–1233.

Binley, A., G. Cassiani, R. Middleton, and P. Winship. 2002. Vadose zone flow model parameterisation using cross-borehole radar and resistivity imaging. J. Hydrol. 267:147–159.

Binley, A., P. Winship, R. Middleton, M. Pokar, and J. West. 2001. High-resolution characterization of vadose zone dynamics using cross-borehole radar. Water Resour. Res. 37:2639–2652.

Brody, A.K., T.M. Palmer, K. Fox-Dobbs, and D.F. Doak. 2010. Termites, vertebrate herbivores, and the fruiting success of *Acacia drepanolobium*. Ecology 91:399–407.

Brooks, R.H., and A.T. Corey. 1964. Hydraulic properties of porous media. Hydrol. Pap. 3. Colorado State Univ., Fort Collins.

Brovelli, A., G. Cassiani, E. Dalla, F. Bergamini, D. Pitea, and A.M. Binley. 2005. Electrical properties of partially saturated sandstones: Novel computational approach with hydrogeophysical applications. Water Resour. Res. 41:W08411, doi:10.1029/2004WR003628.

Campbell, R.B., C.A. Bower, and L.A. Richards. 1948. Change of electrical conductivity with temperature and the relation of osmotic pressure to electrical conductivity and ion concentration for soil extracts. Soil Sci. Soc. Am. Proc. 13:66–69.

Cassiani, G., and A. Binley. 2005. Modeling unsaturated flow in a layered formation under quasi-steady state conditions using geophysical data constraints. Adv. Water Resour. 28:467–477.

Cey, E.E., and D.L. Rudolph. 2009. Field study of macropore flow processes using tension infiltration of a dye tracer in partially saturated soils. Hydrol. Processes 23:1768–1779.

Cey, E.E., D.L. Rudolph, and J. Passmore. 2009. Influence of macroporosity on preferential solute and colloid transport in unsaturated field soils. J. Contam. Hydrol. 107:45–57.

Dahlin, T. 2000. Short note on electrode charge-up effects in DC resistivity data acquisition using multi-electrode arrays. Geophys. Prospect. 48:181–187.

Darlington, J. 2000. Termite nests in a moundfield at Oleserewa, Kenya (Isoptera: Macrotermitinae). Sociobiology 35:25–34.

Darlington, J. 2005. Termite nest structure and impact on the soil at the radar site, Embakasi, Kenya (Isoptera: Termitidae). Sociobiology 45:521–542.

Day-Lewis, F.D., and J.W. Lane. 2004. Assessing the resolution-dependent utility of tomograms for geostatistics. Geophys. Res. Lett. 31:L07503, doi:10.1029/2004GL019617.

Day-Lewis, F.D., K. Singha, and A.M. Binley. 2005. Applying petrophysical models to radar travel time and electrical resistivity tomograms: Resolution-dependent limitations. J. Geophys. Res. 110:B08206, doi:10.1029/2004JB003569.

D'Odorico, P., and A. Porporato (ed.). 2006. Dryland ecohydrology. Springer, Dordrecht, the Netherlands.

Durner, W., U. Jansen, and S.C. Iden. 2008. Effective hydraulic properties of layered soils at the lysimeter scale determined by inverse modelling. Eur. J. Soil Sci. 59:114–124.

Ferré, T., L. Bentley, A. Binley, N. Linde, A. Kemna, K. Singha, K. Holliger, J.A. Huisman, and B. Minsley. 2009. Critical steps for the continuing advancement of hydrogeophysics. EOS Trans. Am. Geophys. Union 90:200.

Fox-Dobbs, K., D.F. Doak, A.K. Brody, and T.M. Palmer. 2010. Termites create spatial structure and govern ecosystem function by affecting N_2 fixation in an East African savanna. Ecology 91:1296–1307.

Friedman, S.P. 2005. Soil properties influencing apparent electrical conductivity: A review. Comput. Electron. Agric. 46:45–70.

Furman, A., T.P.A. Ferré, and G.L. Heath. 2007. Spatial focusing of electrical resistivity surveys considering geologic and hydrologic layering. Geophysics 72:F65–F73.

Furman, A., T.P.A. Ferré, and A.W. Warrick. 2004. Optimization of ERT surveys for monitoring transient hydrological events using perturbation sensitivity and genetic algorithms. Vadose Zone J. 3:1230–1239.

Haberman, R. 1998. Elementary applied partial differential equations with Fourier series and boundary value problems. 3rd ed. Prentice Hall, Upper Saddle River, NJ.

Heiland, C.A. 1940. Geophysical exploration. Prentice Hall, Upper Saddle River, NJ.

Hillel, D. 1998. Environmental soil physics. Academic Press, San Diego.

Hinnell, A.C., T.P.A. Ferré, J.A. Vrugt, J.A. Huisman, S. Moysey, J. Rings, and M.B. Kowalsky. 2010. Improved extraction of hydrologic information from geophysical data through coupled hydrogeophysical inversion. Water Resour. Res. 46:W00D40, doi:10.1029/2008WR007060.

Hubbard, S.S., J.S. Chen, J. Peterson, E.L. Majer, K.H. Williams, D.J. Swift, B. Mailloux, and Y. Rubin. 2001. Hydrogeological characterization of the south oyster bacterial transport site using geophysical data. Water Resour. Res. 37:2431–2456.

Huppert, H.E., and A.W. Woods. 1995. Gravity-driven flows in porous layers. J. Fluid Mech. 292:55–69.

Hvorslev, M.J. 1951. Time lag and soil permeability in ground-water observations. Bull. 36. Waterways Exp. Stn., U.S. Army Corps of Eng., Vicksburg, MS.

Jadoon, K.Z., E. Slob, M. Vanclooster, H. Vereecken, and S. Lambot. 2008. Uniqueness and stability analysis of hydrogeophysical inversion for time-lapse ground-penetrating radar estimates of shallow soil hydraulic properties. Water Resour. Res. 44:W09421, doi:10.1029/2007WR006639.

Jakosky, J.J. 1950. Exploration geophysics. 2nd ed. Trija Publ. Co., Los Angeles.

Koestel, J., A. Kemna, M. Javaux, A. Binley, and H. Vereecken. 2008. Quantitative imaging of solute transport in an unsaturated and undisturbed soil monolith with 3-D ERT and TDR. Water Resour. Res. 44:W12411, doi:10.1029/2007WR006755.

Koestel, J., J. Vanderborght, M. Javaux, A. Kemna, A. Binley, and H. Vereecken. 2009. Noninvasive 3-D transport characterization in a sandy soil using ERT: 1. Investigating the validity of ERT-derived transport parameters. Vadose Zone J. 8:711–722.

Kowalsky, M.B., S. Finsterle, J. Peterson, S. Hubbard, Y. Rubin, E. Majer, A. Ward, and G. Gee. 2005. Estimation of field-scale soil hydraulic and dielectric parameters through joint inversion of GPR and hydrological data. Water Resour. Res. 41:W11425, doi:10.1029/2005WR004237.

Lake, L.W. 1989. Enhanced oil recovery. Prentice Hall, Englewood Cliffs, NJ.

Lambot, S., E.C. Slob, M. Vanclooster, and H. Vereecken. 2006. Closed loop GPR data inversion for soil hydraulic and electric property determination. Geophys. Res. Lett. 33:L21405, doi:10.1029/2006GL027906.

Larsbo, M., S. Roulier, F. Stenemo, R. Kasteel, and N. Jarvis. 2005. An improved dual-permeability model of water flow and solute transport in the vadose zone. Vadose Zone J. 4:398–406.

Leonard, J., E. Perrier, and J.L. Rajot. 2004. Biological macropores effect on runoff and infiltration: A combined experimental and modelling approach. Agric. Ecosyst. Environ. 104:277–285.

Linde, N., A. Binley, A. Tryggvason, L.B. Pedersen, and A. Revil. 2006. Improved hydrogeophysical characterization using joint inversion of cross-hole electrical resistance and ground-penetrating radar traveltime data. Water Resour. Res. 42:W12404, doi:10.1029/2006WR005131.

Looms, M.C., A. Binley, K.H. Jensen, L. Nielsen, and T.M. Hansen. 2008. Identifying unsaturated hydraulic parameters using an integrated data fusion approach on cross-borehole geophysical data. Vadose Zone J. 7:238–248.

Philip, J.R. 1969. Hydrostatics and hydrodynamics in swelling soils. Water Resour. Res. 5:1070–1077.

Pinder, G.F., and M.A. Celia. 2006. Subsurface hydrology. John Wiley & Sons, Hoboken.

Pringle, R.M., D.F. Doak, A.K. Brody, R. Jocque, and T.M. Palmer. 2010. Spatial pattern enhances ecosystem functioning in an African savanna. PLoS Biol. 8(5):e1000377, doi:10.1371/journal.pbio.1000377.

Robinson, D.A., A. Binley, N. Crook, F.D. Day-Lewis, T.P.A. Ferré, V.J.S. Grauch, et al. 2008. Advancing process-based watershed hydrological research using near-surface geophysics: A vision for, and review of, electrical and magnetic geophysical methods. Hydrol. Processes 22:3604–3635.

Rodriguez-Iturbe, I., and A. Porporato. 2004. Ecohydrology of water-controlled ecosystems. Cambridge Univ. Press, New York.

Rubin, Y., and S.S. Hubbard. 2005. Hydrogeophysics. Springer, Dordrecht, the Netherlands.

Rucker, D.F., and T.P.A. Ferré. 2004. Parameter estimation for soil hydraulic properties using zero-offset borehole radar: Analytical method. Soil Sci. Soc. Am. J. 68:1560–1567.

Rucker, D.F., A.W. Warrick, and T.P.A. Ferré. 2005. Parameter equivalence for the Gardner and van Genuchten soil hydraulic conductivity functions for steady vertical flow with inclusions. Adv. Water Resour. 28:689–699.

Sakaki, T., and T.H. Illangasekare. 2007. Comparison of height-averaged and point-measured capillary pressure-saturation relations for sands using a modified Tempe cell. Water Resour. Res. 43:W12502, doi:10.1029/2006WR005814.

Samouelian, A., I. Cousin, A. Tabbagh, A. Bruand, and G. Richard. 2005. Electrical resistivity survey in soil science: A review. Soil Tillage Res. 83:173–193.

Sidle, R.C., S. Noguchi, Y. Tsuboyama, and K. Laursen. 2001. A conceptual model of preferential flow systems in forested hillslopes: Evidence of self-organization. Hydrol. Processes 15:1675–1692.

Šimůnek, J., M.Th. van Genuchten, and M. Šejna. 2006. The HYDRUS software package for simulating the two- and three-dimensional movement of water, heat, and multiple solutes in variably-saturated media. User manual, version 1.0. PC-Progress, Prague, Czech Republic.

Šimůnek, J., M.Th. van Genuchten, and M. Šejna. 2008. Development and applications of the HYDRUS and STANMOD software packages and related codes. Vadose Zone J. 7:587–600.

Slater, L.D., and A. Reeve. 2002. Investigating peatland stratigraphy and hydrogeology using integrated electrical geophysics. Geophysics 67:365–378.

Szalai, S., and L. Szarka. 2008. On the classification of surface geoelectric arrays. Geophys. Prospect. 56:159–175.

Telford, W.M., L.P. Geldart, and R.E. Sheriff. 1990. Applied geophysics. 2nd ed. Cambridge Univ. Press, New York.

Thomasson, M.J., P.J. Wierenga, and T.P.A. Ferré. 2006. A field application of the scaled-predictive method for unsaturated soil. Vadose Zone J. 5:1093–1109.

Topp, G.C., J.L. Davis, and A.P. Annan. 1980. Electromagnetic determination of soil water content: Measurements in coaxial transmission lines. Water Resour. Res. 16:574–582.

Tracy, F.T. 1995. 1-D, 2-D, and 3-D analytical solutions of unsaturated flow in groundwater. J. Hydrol. 170:199–214.

Tsuboyama, Y., R.C. Sidle, S. Noguchi, and I. Hosoda. 1994. Flow and solute transport through the soil matrix and macropores of a hillslope segment. Water Resour. Res. 30:879–890.

Turner, S.J. 2006. Termites as mediators of the water economy of arid savanna ecosystems. p. 341. *In* P. D'Odorico and A. Porporato (ed.) Dryland ecohydrology. Springer, Dordrecht, the Netherlands.

Vereecken, H., J.A. Huisman, H. Bogena, J. Vanderborght, J.A. Vrugt, and J.W. Hopmans. 2008. On the value of soil moisture measurements in vadose zone hydrology: A review. Water Resour. Res. 44:W00D06, doi:10.1029/2008WR006829.

Weiler, M., and H. Flühler. 2004. Inferring flow types from dye patterns in macroporous soils. Geoderma 120:137–153.

Weiler, M., and F. Naef. 2003a. An experimental tracer study of the role of macropores in infiltration in grassland soils. Hydrol. Processes 17:477–493.

Weiler, M., and F. Naef. 2003b. Simulating surface and subsurface initiation of macropore flow. J. Hydrol. 273:139–154.

Williams, C.A., and J.D. Albertson. 2004. Soil moisture controls on canopy-scale water and carbon fluxes in an African savanna. Water Resour. Res. 40:W09302, doi:10.1029/2004WR003208.

Wu, Y.S., and L.H. Pan. 2005. An analytical solution for transient radial flow through unsaturated fractured porous media. Water Resour. Res. 41:W02029, doi:10.1029/2004WR003107.